

The initial conditions of star formation VIII: an observational study of the Ophiuchus cloud L1688 and implications for the prestellar core mass function

R. J. Simpson, D. Nutter and D. Ward-Thompson

School of Physics and Astronomy, Cardiff University, The Parade, Cardiff, CF24 3AA

2008 July 8

ABSTRACT

We re-analyse all of the archive observations of the Ophiuchus dark cloud L1688 that were carried out with the submillimetre common-user bolometer array (SCUBA) at the James Clerk Maxwell Telescope (JCMT). For the first time we put together all of the data that were taken of this cloud at different times to make a deeper map at 850 μ m than has ever previously been published. Using this new, deeper map we extract the pre-stellar cores from the data. We use updated values for the distance to the cloud complex, and also for the internal temperatures of the pre-stellar cores to generate an updated core mass function (CMF). This updated CMF is consistent with previous results in so far as they went, but our deeper map gives an improved completeness limit of 0.1M_⊙ (0.16 Jy), which enables us to show that a turnover exists in the low-mass regime of the CMF. The L1688 CMF shows the same form as the stellar IMF and can be mapped onto the stellar IMF, showing that the IMF is determined at the prestellar core stage. We compare L1688 with the Orion star-forming region and find that the turnover in the L1688 CMF occurs at a mass roughly a factor of two lower than the CMF turnover in Orion. This suggests that the position of the CMF turnover may be a function of environment.

Key words: stars: formation – ISM: dust – infrared: ISM – submillimetre: ISM

1 INTRODUCTION

Star formation in molecular clouds occurs within prestellar cores, which are gravitationally bound cores within the clouds (Ward-Thompson et al. 1994; Andre, Ward-Thompson, & Motte 1996; Ward-Thompson, Motte, & Andre 1999; Ward-Thompson 2002; Di Francesco et al. 2007; Ward-Thompson et al. 2007a).

A number of observations have shown that the core mass function (CMF) of prestellar cores appears to mimic (Motte Andre & Neri 1998, hereafter MAN98, Testi & Sargent 1998; Johnstone et al. 2000; Motte et al. 2001; Johnstone et al. 2001; Kroupa 2002; Onishi et al. 2002; Johnstone, Matthews, & Mitchell 2006) the stellar initial mass function (IMF; Salpeter 1955).

However, the comparison between the core mass function and stellar IMF has not often been accurately probed at lower masses. It is more difficult to study this part of the mass domain, but recent results have shown that the CMF exhibits a turnover at lower masses in a manner similar to the IMF (Nutter & Ward-Thompson 2007).

The Ophiuchus star-forming region is located at a dis-

tance of 139 pc (Mamajek 2008) and is a site of low-mass star formation (Wilking & Lada 1983). The region consists of two main clouds, L1688 and L1689, which both have extended streamers leading out to lengths of around 10 pc (Loren 1989). Specifically, it is the more massive of the two clouds, L1688, which is studied in this paper, and which is generally known as the Ophiuchus main cloud. Very high star formation rates have been measured here, with 14–40% of the molecular gas being converted into stars (Vrba 1977).

The Ophiuchus cloud has been observed in many wavelengths from the visible to the submillimetre (e.g. MAN98, Montmerle et al. 1983; Wilking, Lada, & Young 1989; Andre et al. 1992; Greene & Young 1992; Barsony et al. 1997; Johnstone et al. 2000; Jessop & Ward-Thompson 2001; Johnstone, Di Francesco & Kirk 2004; Di Francesco et al. 2008). Because of this, the properties of the cloud are very well known and it is therefore a good place to probe low-mass star formation.

The Ophiuchus cloud is the nearest example of ‘clustered’ star formation (MAN98). This is important to study because most stars form in clustered environments (Zinnecker, McCaughrean, & Wilking 1993). Ophiuchus may also be the nearest example

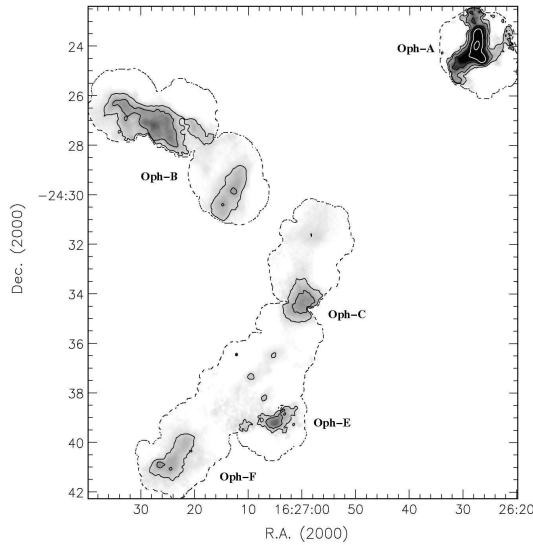


Figure 2. Greyscale image and isophotal contour map of the SCUBA 850 μm continuum jiggle map data of the Ophiuchus dark cloud L1688. Contours at 0.25, 0.5 and 1.0 Jy/beam are shown in black; 2.0 and 4.0 Jy/beam contours are shown in white. 1σ noise levels vary from 10 to 180 mJy/beam.

of triggered star formation in action (Loren 1989; Nutter, Ward-Thompson, & André 2006), making it a prime candidate for study.

In this study we have combined all of the high signal-to-noise SCUBA wide-field scan-map data and narrow-field jiggle-map data taken of L1688, and re-reduced it to produce the deepest submillimetre map of this cloud ever made. L1688 is the region of the Ophiuchus cloud defined by Loren (1989) and outlined in their Figure 1a (it is marked out by a solid, 5K contour). Of the original regions covered at 1.3mm by MAN98 (Oph-A, -B, -C, -D, -E and -F) only one, Oph-D, is not included here, as it is not part of the central region of L1688. A newly discovered region, which we name Oph-J, is discussed. Two smaller regions, Oph-H and Oph-I are discussed by Johnstone, Di Francesco & Kirk (2004) but are not included in this study. We produce a CMF and investigate the low-mass end of the CMF of the cloud. We compare this with previous findings and also with the Orion molecular cloud (Nutter & Ward-Thompson 2007).

2 OBSERVATIONS

The submillimetre data presented in this study were obtained using the Submillimetre Common User Bolometer Array (SCUBA) on the James Clerk Maxwell Telescope (JCMT). SCUBA used a dichroic beam-splitter to simultaneously observe at 850 μm and 450 μm wavelengths at resolutions of 14 arcsec and 8 arcsec respectively. The data presented here were acquired from the Canadian Astronomy Data Center's JCMT data archive (Tilanus et al. 1997). Some of these data have been published previously (Johnstone et al. 2000; Johnstone, Di Francesco & Kirk 2004; Di Francesco et al. 2008) but have all been consistently re-reduced here using a single method for this study. Some data from these stud-

ies has been omitted where the mapping technique is low signal-to-noise. Only the 850 μm data have been used and are presented here.

SCUBA was used in scan-map mode to produce the observations in Figure 1. To acquire a scan-map, the SCUBA array was scanned across the sky at 15.5° to the main axis to achieve Nyquist sampling. It was then able to raster across the sky in this mode and achieve maps several arcminutes across (Jenness et al. 2000).

The scan-map data consist of 76 observations over 3 nights at the JCMT on 1998 July 11 and 12, and 1999 March 4 (see Table 1). The sky opacity at 850 μm varied from 0.10 to 0.29 with a mean value of 0.17, as determined by the 'skydip' method (Archibald et al. 2002). The data were reduced using the SCUBA User Reduction Facility (Jenness et al. 2000) and calibrated using observations of Uranus or Mars or of the secondary calibrator CRL618 (Sandell 1994).

The scan-map observation mode results in differential maps which must be reconstructed. This is done in Fourier space using the Emerson-2 method (Emerson & Payne 1995; Sandell, Jessop & Jenness 2001). Baseline offsets were removed using the SURF command SCAN_RLB with the 'median' method (Jenness et al. 2000). The time-series data were checked for each observation and noisy bolometers were removed by eye. We estimate that the calibration uncertainty is $\pm 10\%$ based on the variation in the calibration factors from Uranus and Mars across all the datasets (see Tables 4 and 5).

The data make up one map which is split into 7 regions, following the naming methodology in MAN98. Figure 1 shows the whole map with the individual regions named. Johnstone et al. (2000) first published the 850 μm scan-map data used in this study. They found good agreement with the results of MAN98.

SCUBA was used in jiggle-map mode for the observations in Figure 2. The jiggle-map data consist of 42 observations over 19 nights at the JCMT between 1997 August 7 and 2004 March 29 (see Table 1). The sky opacity at 850 μm varied from 0.21 to 0.52 with a mean value of 0.30, as determined by the 'skydip' method. The jiggle-map data were also reduced using the SCUBA User Reduction Facility and calibrated using observations of Uranus or Mars or of the secondary calibrator CRL618. These data are shown in Figure 2. A close-up of each of the main regions is shown in Figure 3.

3 RESULTS

The final map was created from data taken over a range of dates and weather conditions at the JCMT. To produce a final map, with quantified noise levels, we use the technique from Nutter & Ward-Thompson (2007). The fluxes quoted in Table 2 are the result of combining the scan- and jiggle-map data. The fluxes from coincident scan- and jiggle-map sources were combined using the noise in each map as a weighting factor.

In this technique the bright sources are masked before smoothing the map to remove the large-scale structure. This is then subtracted from the original data. The resultant map is then used to create a noise map by measuring the standard

Table 2. Source names, peak positions, 850- μ m peak flux densities and signal-to-noise ratios of the cores in regions Oph-A, -B, -C, -E, -F, -J. The flux densities $S_{1.3mm}^{peak}$ and S_{850}^{peak} refer to the MAN98 peak flux and the peak flux in our dataset respectively.

Source Name	MAN98 Position		SCUBA Position		Flux Densities			S/N (σ)	IR assn
	RA (2000)	Dec. (2000)	RA (2000)	Dec (2000)	$S_{1.3mm}^{peak}$ (mJy/beam)	S_{850}^{peak} (mJy/beam)			
A-MM1	16 ^h 26 ^m 22.44 ^s	-24 ^o 23'40.26"	16 ^h 26 ^m 23.00 ^s	-24 ^o 23'34.46"	50 \pm 15	380 \pm 15	23		
A-MM2/3	—	—	16 ^h 26 ^m 23.80 ^s	-24 ^o 24'09.95"	—	660 \pm 25	24		
A-MM4	16 ^h 26 ^m 24.40 ^s	-24 ^o 21'52.13"	16 ^h 26 ^m 24.14 ^s	-24 ^o 21'59.30"	80 \pm 15	930 \pm 20	42		
A-MM5	16 ^h 26 ^m 26.42 ^s	-24 ^o 22'27.00"	16 ^h 26 ^m 26.66 ^s	-24 ^o 22'28.60"	100 \pm 20	1590 \pm 20	71		
A-MM6	16 ^h 26 ^m 28.43 ^s	-24 ^o 22'52.86"	16 ^h 26 ^m 28.21 ^s	-24 ^o 23'00.10"	200 \pm 25	4050 \pm 30	138		
A-MM7	16 ^h 26 ^m 29.42 ^s	-24 ^o 22'33.80"	16 ^h 26 ^m 29.45 ^s	-24 ^o 22'33.01"	110 \pm 30	1770 \pm 30	60		
A-MM8	16 ^h 26 ^m 33.48 ^s	-24 ^o 25'00.53"	16 ^h 26 ^m 31.80 ^s	-24 ^o 24'50.00"	80 \pm 25	6110 \pm 25	245		
A-MM9	—	—	16 ^h 26 ^m 45.18 ^s	-24 ^o 23'10.02"	—	490 \pm 30	16	Y	
A-MM10	—	—	16 ^h 26 ^m 21.83 ^s	-24 ^o 22'51.96"	—	1640 \pm 25	66	Y	
A-MM11	—	—	16 ^h 26 ^m 32.74 ^s	-24 ^o 26'14.40"	—	1240 \pm 25	50		
A-MM12	—	—	16 ^h 26 ^m 14.24 ^s	-24 ^o 25'04.33"	—	870 \pm 25	35		
A-MM15	—	—	16 ^h 26 ^m 40.50 ^s	-24 ^o 27'16.28"	—	20 \pm 30	1	Y	
A-MM16	—	—	16 ^h 26 ^m 36.26 ^s	-24 ^o 28'12.84"	—	60 \pm 20	3		
A-MM17	—	—	16 ^h 26 ^m 34.77 ^s	-24 ^o 28'08.10"	—	60 \pm 20	3		
A-MM18	—	—	16 ^h 26 ^m 43.73 ^s	-24 ^o 17'25.74"	—	1680 \pm 30	56		
A-MM19	—	—	16 ^h 26 ^m 24.30 ^s	-24 ^o 16'16.11"	—	430 \pm 40	11	Y	
A-MM20	—	—	16 ^h 26 ^m 36.18 ^s	-24 ^o 17'56.34"	—	240 \pm 30	8		
A-MM21	—	—	16 ^h 26 ^m 31.64 ^s	-24 ^o 18'38.05"	—	410 \pm 35	12		
A-MM22	—	—	16 ^h 26 ^m 31.45 ^s	-24 ^o 18'52.05"	—	210 \pm 35	6		
A-MM23	—	—	16 ^h 26 ^m 07.89 ^s	-24 ^o 20'30.50"	—	2370 \pm 25	95		
A-MM24	—	—	16 ^h 26 ^m 10.50 ^s	-24 ^o 20'56.83"	—	760 \pm 25	30	Y	
A-MM25	—	—	16 ^h 25 ^m 55.96 ^s	-24 ^o 20'49.47"	—	140 \pm 30	5	Y	
A-MM26	—	—	16 ^h 26 ^m 15.40 ^s	-24 ^o 25'32.50"	—	820 \pm 25	33		
A-MM27	—	—	16 ^h 26 ^m 13.85 ^s	-24 ^o 25'25.16"	—	650 \pm 25	26		
A-MM28	—	—	16 ^h 26 ^m 54.75 ^s	-24 ^o 19'16.55"	—	410 \pm 40	10		
A-MM29	—	—	16 ^h 26 ^m 53.36 ^s	-24 ^o 19'28.08"	—	350 \pm 40	9		
A-MM30	—	—	16 ^h 26 ^m 09.63 ^s	-24 ^o 19'43.25"	—	2460 \pm 20	123		
A2-MM1	16 ^h 26 ^m 11.45 ^s	-24 ^o 24'40.00"	16 ^h 26 ^m 11.73 ^s	-24 ^o 24'54.16"	60 \pm 10	640 \pm 20	32		
A3-MM1	16 ^h 26 ^m 09.41 ^s	-23 ^o 24'06.13"	16 ^h 26 ^m 10.07 ^s	-24 ^o 23'11.00"	90 \pm 10	640 \pm 30	21		
A-N	16 ^h 26 ^m 21.35 ^s	-24 ^o 19'40.33"	16 ^h 26 ^m 22.74 ^s	-24 ^o 20'00.00"	60 \pm 10	410 \pm 30	14		
A-S	—	—	16 ^h 26 ^m 42.69 ^s	-24 ^o 26'08.05"	85 \pm 10	10 \pm 35	0		
SM1	16 ^h 26 ^m 27.45 ^s	-24 ^o 23'55.93"	16 ^h 26 ^m 27.73 ^s	-24 ^o 23'58.17"	1300 \pm 20	14140 \pm 25	571		
SM1N	16 ^h 26 ^m 27.44 ^s	-24 ^o 23'27.93"	16 ^h 26 ^m 27.46 ^s	-24 ^o 23'32.71"	790 \pm 25	5600 \pm 15	359		
SM2	16 ^h 26 ^m 29.46 ^s	-24 ^o 24'25.91"	16 ^h 26 ^m 29.41 ^s	-24 ^o 24'26.69"	450 \pm 30	11490 \pm 15	690		
VLA1623	—	—	16 ^h 26 ^m 26.74 ^s	-24 ^o 24'30.00"	—	5630 \pm 30	188		
B1-MM1	16 ^h 27 ^m 08.57 ^s	-24 ^o 27'50.19"	16 ^h 27 ^m 09.32 ^s	-24 ^o 27'43.73"	50 \pm 5	50 \pm 30	2		
B1-MM2	16 ^h 27 ^m 11.60 ^s	-24 ^o 29'17.99"	16 ^h 27 ^m 12.23 ^s	-24 ^o 29'23.65"	45 \pm 10	2140 \pm 10	230		
B1-MM3	16 ^h 27 ^m 12.62 ^s	-24 ^o 29'57.92"	16 ^h 27 ^m 12.60 ^s	-24 ^o 29'49.89"	65 \pm 10	4140 \pm 10	446		
B1-MM4	16 ^h 27 ^m 15.64 ^s	-24 ^o 30'41.72"	16 ^h 27 ^m 15.32 ^s	-24 ^o 30'36.82"	60 \pm 15	3330 \pm 10	372		
B1-MM5	—	—	16 ^h 27 ^m 16.05 ^s	-24 ^o 31'09.30"	—	650 \pm 25	26	Y	
B1-MM6	—	—	16 ^h 27 ^m 10.58 ^s	-24 ^o 28'54.69"	—	350 \pm 30	12		
B1-MM7	—	—	16 ^h 27 ^m 18.72 ^s	-24 ^o 30'24.64"	—	180 \pm 30	6		
B1B2-MM1	16 ^h 27 ^m 11.57 ^s	-24 ^o 27'38.99"	16 ^h 27 ^m 12.44 ^s	-24 ^o 27'30.31"	40 \pm 5	350 \pm 35	10		
B1B2-MM2	16 ^h 27 ^m 17.60 ^s	-24 ^o 28'47.59"	16 ^h 27 ^m 17.77 ^s	-24 ^o 28'59.75"	45 \pm 10	490 \pm 10	51	Y	
B2-MM2	16 ^h 27 ^m 20.56 ^s	-24 ^o 27'08.39"	16 ^h 27 ^m 19.82 ^s	-24 ^o 27'13.87"	85 \pm 10	1390 \pm 20	79		
B2-MM4	16 ^h 27 ^m 24.58 ^s	-24 ^o 27'45.12"	16 ^h 27 ^m 24.50 ^s	-24 ^o 27'46.30"	90 \pm 15	1520 \pm 20	86		
B2-MM5	16 ^h 27 ^m 24.57 ^s	-24 ^o 27'26.12"	16 ^h 27 ^m 24.74 ^s	-24 ^o 27'29.29"	100 \pm 15	1810 \pm 20	102		
B2-MM6	16 ^h 27 ^m 25.57 ^s	-24 ^o 27'00.05"	16 ^h 27 ^m 25.57 ^s	-24 ^o 26'58.19"	150 \pm 15	2570 \pm 20	134		
B2-MM7	16 ^h 27 ^m 27.58 ^s	-24 ^o 27'38.92"	16 ^h 27 ^m 27.70 ^s	-24 ^o 27'38.86"	100 \pm 20	990 \pm 25	39		
B2-MM8	16 ^h 27 ^m 27.57 ^s	-24 ^o 27'06.92"	16 ^h 27 ^m 27.96 ^s	-24 ^o 27'06.85"	215 \pm 20	3140 \pm 20	178		
B2-MM9	16 ^h 27 ^m 28.56 ^s	-24 ^o 26'36.85"	16 ^h 27 ^m 28.82 ^s	-24 ^o 26'38.59"	110 \pm 15	2170 \pm 20	113		
B2-MM10	16 ^h 27 ^m 29.58 ^s	-24 ^o 27'41.78"	16 ^h 27 ^m 29.53 ^s	-24 ^o 27'40.85"	160 \pm 10	1020 \pm 25	41	Y	
B2-MM13	16 ^h 27 ^m 32.55 ^s	-24 ^o 26'06.58"	16 ^h 27 ^m 32.95 ^s	-24 ^o 26'03.16"	75 \pm 15	780 \pm 30	26		
B2-MM14	16 ^h 27 ^m 32.56 ^s	-24 ^o 26'28.58"	16 ^h 27 ^m 32.58 ^s	-24 ^o 26'27.46"	130 \pm 15	1990 \pm 15	128		
B2-MM15	16 ^h 27 ^m 32.57 ^s	-24 ^o 27'02.58"	16 ^h 27 ^m 32.87 ^s	-24 ^o 26'59.16"	90 \pm 15	990 \pm 30	33		
B2-MM16	16 ^h 27 ^m 34.56 ^s	-24 ^o 26'12.45"	16 ^h 27 ^m 34.62 ^s	-24 ^o 26'16.39"	100 \pm 15	2090 \pm 15	134		

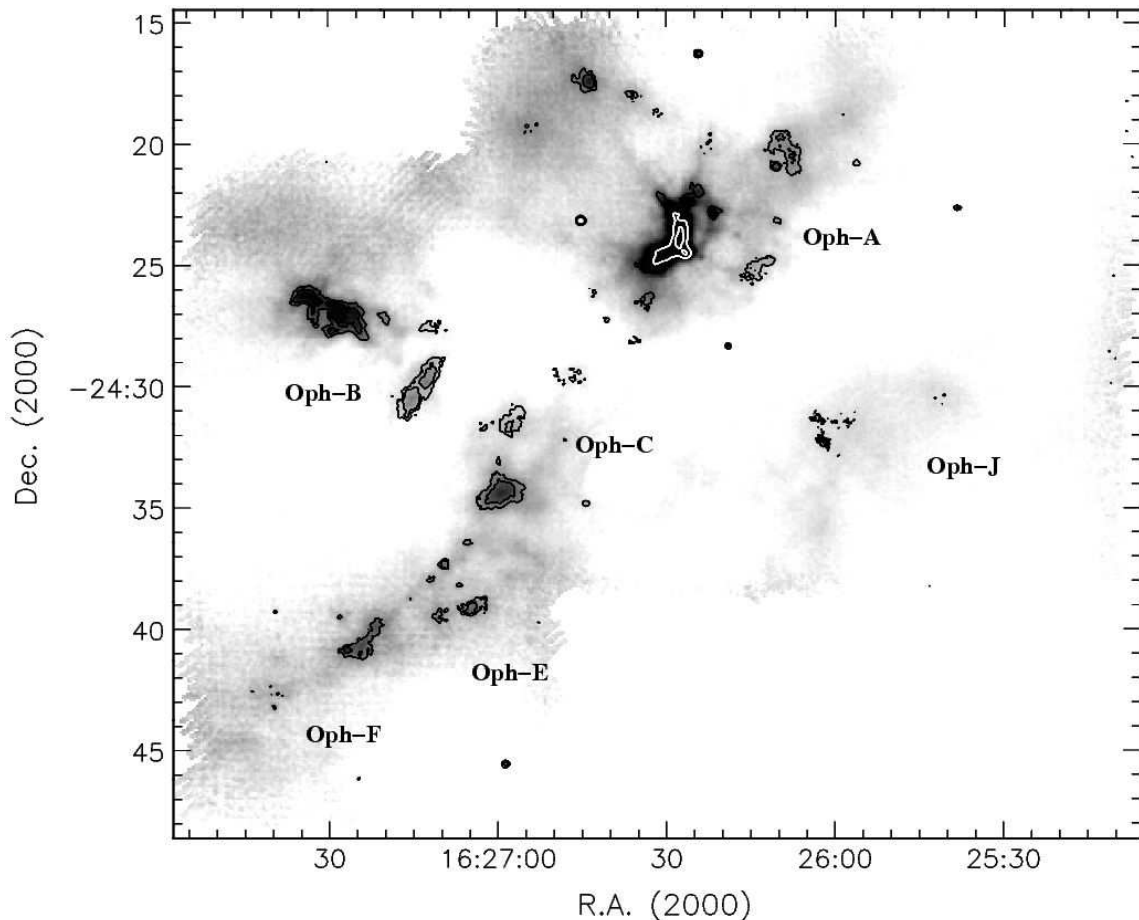


Figure 1. Greyscale image and isophotal contour map of the SCUBA 850 μ m continuum scan-map data of the Ophiuchus dark cloud L1688. Signal-to-noise contours at 5 σ and 10 σ are shown in black; 25 σ and 100 σ contours shown in white. 1 σ noise levels vary from 15 to 40 mJy/beam (see text for details).

Table 1. Details of observations.

Date	Mode	$\overline{\tau}_{850}$	No. of Datasets
1997 Aug 07	Jiggle Map	0.285	1
1997 Aug 08	Jiggle Map	0.282	1
1997 Aug 09	Jiggle Map	0.280	5
1997 Aug 10	Jiggle Map	0.220	1
1997 Aug 11	Jiggle Map	0.103	1
1997 Aug 25	Jiggle Map	0.206	2
1997 Aug 26	Jiggle Map	0.183	2
1997 Sep 09	Jiggle Map	0.108	6
1998 Jun 26	Jiggle Map	0.278	2
1998 Jul 11	Scan Map	0.103	27
1998 Jul 12	Scan Map	0.148	24
1998 Aug 11	Jiggle Map	0.211	2
1998 Aug 25	Jiggle Map	0.314	2
1999 Mar 04	Scan Map	0.205	25
1999 Mar 13	Jiggle Map	0.208	2
1999 Aug 20	Jiggle Map	0.279	2
2000 Aug 08	Jiggle Map	0.208	1
2001 Jul 31	Jiggle Map	0.310	3
2003 Feb 04	Jiggle Map	0.260	8
2004 Mar 29	Jiggle Map	0.255	1

deviation of the pixel values in a series of 50 arcsec apertures. The gaps from the bright sources are filled in by simple interpolation between the edge values.

The resultant noise map is shown in Figure 4. It can be seen that the south and north-east corners of the map have a higher level of noise. These are the two regions containing the least number of observations. The noise in the whole map ranges from 15 to 40 mJy beam $^{-1}$ with a median value of 25 mJy beam $^{-1}$.

A signal-to-noise map was created by dividing the data map by the noise map. Sources were identified with the method from Nutter & Ward-Thompson (2007), in which the signal-to-noise map is used along with the following set of criteria. Any sources with a peak flux density of 5 σ or more were taken to be real. A dip of at least 3 σ was required between two adjacent peaks for those two peaks to be identified as two separate sources.

The 3 σ contour from the signal-to-noise map was used to draw an elliptical aperture around each identified source on the data. The flux density for any given source was then derived using this 3 σ aperture and a ‘sky’ aperture of the same size placed on a nearby area in the map containing no significant emission. The locations of each core from each region are given in Table 2. Also given in these tables are the equivalent fluxes from MAN98.

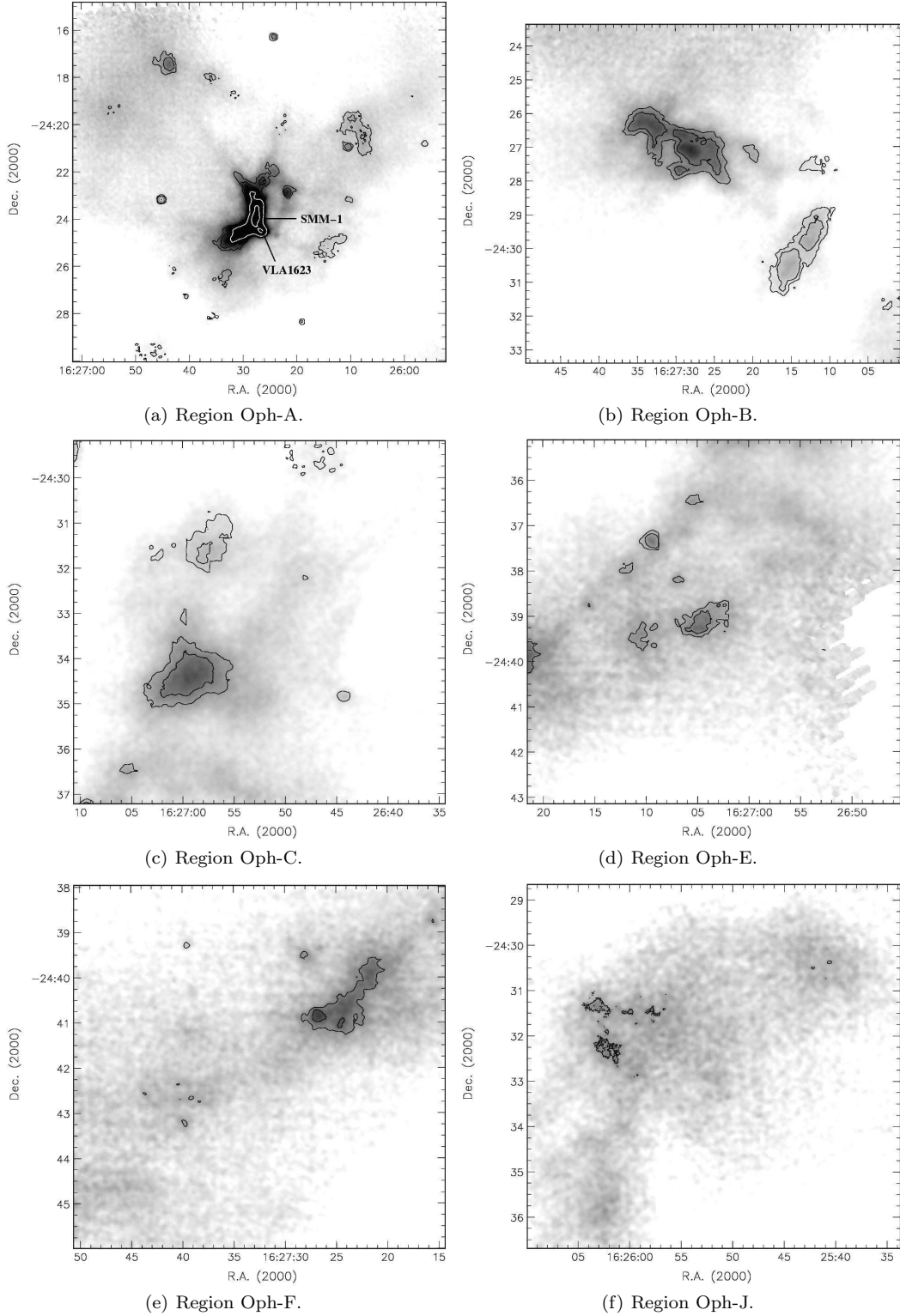
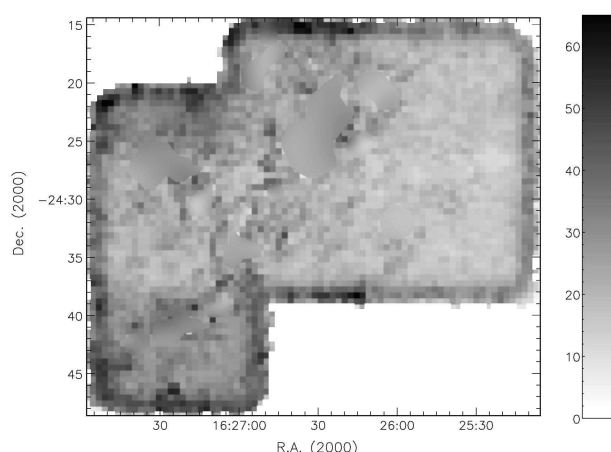


Figure 3. 850 μ m continuum maps of regions Oph-A, B, C, E, F and new region J. Signal-to-noise contours at 5 σ and 10 σ are shown in black; 25 σ and 100 σ contours are shown in white.

Table 2 – continued Core properties.

Source Name	MAN98 Position		SCUBA Position		Flux Densities		S/N (σ)	IR assn
	RA (2000)	Dec. (2000)	RA (2000)	Dec (2000)	$S_{1.3mm}^{peak}$ (mJy/beam)	S_{850}^{peak} (mJy/beam)		
C-MM2	16 ^h 26 ^m 58.69 ^s	-24 [°] 33'52.85"	16 ^h 26 ^m 59.75 ^s	-24 [°] 33'56.95"	45 ± 10	1760 ± 25	70	
C-MM3	16 ^h 26 ^m 58.70 ^s	-24 [°] 34'21.85"	16 ^h 26 ^m 58.80 ^s	-24 [°] 34'23.40"	55 ± 25	2260 ± 20	106	
C-MM5	16 ^h 26 ^m 59.70 ^s	-24 [°] 34'26.79"	16 ^h 26 ^m 59.61 ^s	-24 [°] 34'26.81"	50 ± 25	1970 ± 20	93	
C-MM6	16 ^h 27 ^m 01.71 ^s	-24 [°] 34'36.65"	16 ^h 27 ^m 01.58 ^s	-24 [°] 34'44.62"	60 ± 20	1670 ± 20	79	
C-MM8	—	—	16 ^h 26 ^m 49.09 ^s	-24 [°] 29'45.15"	—	240 ± 35	7	
C-MM9	—	—	16 ^h 26 ^m 48.10 ^s	-24 [°] 32'12.50"	—	90 ± 30	3	
C-MM10	—	—	16 ^h 27 ^m 02.26 ^s	-24 [°] 31'42.56"	—	580 ± 25	23	
C-MM11	—	—	16 ^h 26 ^m 44.27 ^s	-24 [°] 34'50.43"	—	110 ± 30	4	Y
C-MM12	—	—	16 ^h 26 ^m 59.80 ^s	-24 [°] 33'08.75"	—	150 ± 30	5	
C-N	16 ^h 26 ^m 57.64 ^s	-24 [°] 31'38.92"	16 ^h 26 ^m 58.11 ^s	-24 [°] 31'46.32"	60 ± 10	2540 ± 25	105	
E-MM2a	16 ^h 27 ^m 01.59 ^s	-24 [°] 38'28.66"	16 ^h 27 ^m 02.89 ^s	-24 [°] 38'46.47"	50 ± 15	200 ± 40	5	
E-MM2b	16 ^h 27 ^m 01.80 ^s	-24 [°] 38'51.65"	16 ^h 27 ^m 02.19 ^s	-24 [°] 39'11.49"	60 ± 15	250 ± 40	6	
E-MM2d	16 ^h 27 ^m 04.81 ^s	-24 [°] 39'15.45"	16 ^h 27 ^m 04.64 ^s	-24 [°] 39'15.63"	110 ± 20	660 ± 40	17	
E-MM4	16 ^h 27 ^m 10.82 ^s	-24 [°] 39'30.05"	16 ^h 27 ^m 10.67 ^s	-24 [°] 39'25.28"	50 ± 10	490 ± 40	13	
E-MM5	16 ^h 27 ^m 11.79 ^s	-24 [°] 37'56.98"	16 ^h 27 ^m 11.67 ^s	-24 [°] 37'57.46"	55 ± 10	440 ± 30	14	
E-MM6	—	—	16 ^h 27 ^m 09.46 ^s	-24 [°] 37'20.92"	—	310 ± 35	9	Y
E-MM7	—	—	16 ^h 27 ^m 05.45 ^s	-24 [°] 36'27.02"	—	200 ± 30	7	Y
E-MM8	—	—	16 ^h 27 ^m 04.19 ^s	-24 [°] 39'02.59"	—	300 ± 30	10	
E-MM9	—	—	16 ^h 27 ^m 06.84 ^s	-24 [°] 38'11.38"	—	140 ± 30	5	Y
E-MM10	—	—	16 ^h 27 ^m 15.55 ^s	-24 [°] 38'45.95"	—	100 ± 40	3	Y
F-MM1	16 ^h 27 ^m 21.84 ^s	-24 [°] 39'59.31"	16 ^h 27 ^m 21.49 ^s	-24 [°] 39'54.38"	65 ± 20	1660 ± 20	74	
F-MM2a	16 ^h 27 ^m 23.86 ^s	-24 [°] 40'35.18"	16 ^h 27 ^m 24.43 ^s	-24 [°] 40'34.79"	—	1760 ± 25	69	
F-MM2b	16 ^h 27 ^m 23.86 ^s	-24 [°] 40'35.18"	16 ^h 27 ^m 24.69 ^s	-24 [°] 41'04.03"	—	1220 ± 25	48	Y
F-MM3	—	—	16 ^h 27 ^m 26.69 ^s	-24 [°] 40'51.71"	—	1080 ± 35	31	Y
F-MM4	—	—	16 ^h 27 ^m 28.20 ^s	-24 [°] 39'30.17"	—	310 ± 35	9	Y
F-MM5	—	—	16 ^h 27 ^m 39.62 ^s	-24 [°] 39'15.26"	—	130 ± 35	4	Y
F-MM6	—	—	16 ^h 27 ^m 43.73 ^s	-24 [°] 42'34.59"	—	150 ± 40	4	
F-MM7	—	—	16 ^h 27 ^m 39.81 ^s	-24 [°] 43'12.25"	—	190 ± 40	5	Y
F-MM8	—	—	16 ^h 27 ^m 39.22 ^s	-24 [°] 42'39.77"	—	330 ± 40	8	
F-MM9	—	—	16 ^h 27 ^m 40.46 ^s	-24 [°] 42'20.22"	—	150 ± 40	4	
J-MM1	—	—	16 ^h 26 ^m 19.12 ^s	-24 [°] 28'20.14"	—	60 ± 15	4	Y
J-MM2	—	—	16 ^h 26 ^m 02.17 ^s	-24 [°] 32'25.49"	—	670 ± 25	27	
J-MM3	—	—	16 ^h 26 ^m 03.45 ^s	-24 [°] 31'20.50"	—	550 ± 25	22	
J-MM4	—	—	16 ^h 25 ^m 59.95 ^s	-24 [°] 31'29.82"	—	280 ± 20	14	
J-MM5	—	—	16 ^h 25 ^m 40.64 ^s	-24 [°] 30'22.68"	—	250 ± 20	13	
J-MM6	—	—	16 ^h 25 ^m 42.25 ^s	-24 [°] 30'29.70"	—	120 ± 25	5	
J-MM7	—	—	16 ^h 25 ^m 38.39 ^s	-24 [°] 22'37.82"	—	100 ± 35	3	Y

**Figure 4.** The 850 μ m noise-map for the Ophiuchus dark cloud L1688. The scale bar shown is in units of mJy/beam.

The only places on the map where this method for characterizing cores does not apply is when the cores lie on, or adjacent to, bright emission. In these cases, such as cores next to SM1 in Rho Oph-A (Ward-Thompson et al. 1989), apertures were drawn following contours on the data map corresponding to the true 3σ value and the flux density divided in proportion to the peak fluxes of the cores within areas of bright emission. We found 93 cores, 21 of which had an infrared source associated with them, as identified by Spitzer as part of the c2d surveys (Enoch et al. 2008; Jorgensen et al. 2008). These latter cores were discounted in our subsequent analysis as not being prestellar.

Johnstone, Di Francesco & Kirk (2004) mapped a large area around L1688 using a ‘fast-mapping’ method. This technique is different to the standard scan-mapping method and results in lower signal-to-noise data. In order to produce a consistently reduced map using our method, we therefore ignored the non-standard data. However,

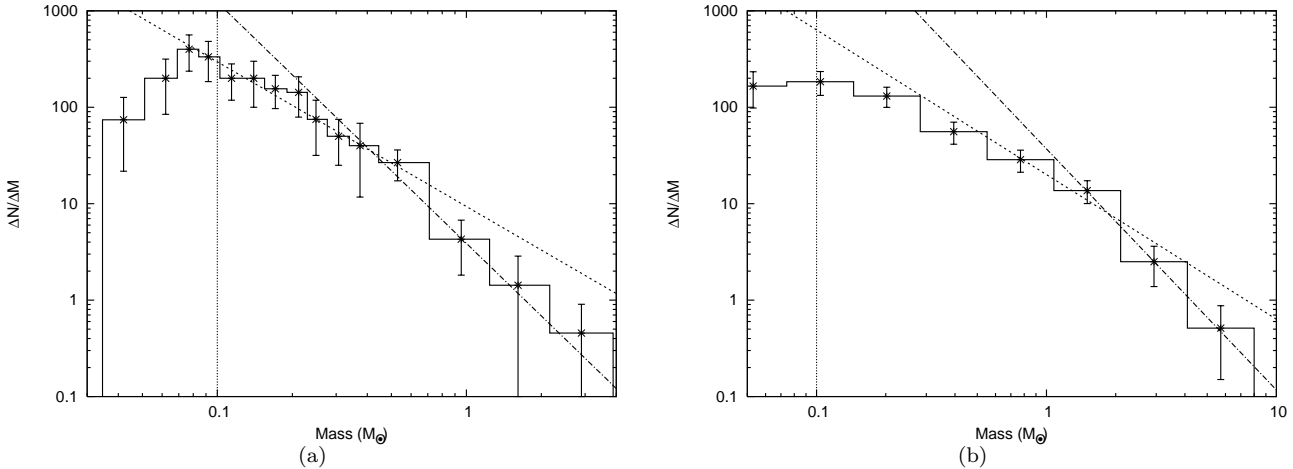


Figure 5. Comparison of 1.3mm and 850μm datasets. (a) Graph of $(\Delta N / \Delta M)$ against mass for L1688, recreated from MAN98 1.3mm data for comparison with data from this study. (b) Equivalent graph using SCUBA 850μm data from JCMT archive. In each plot, the vertical dashed line shows the completeness limit of the study. The two semi-dashed lines on each plot show fits of the two power law slopes from the higher-mass end of the IMF (see text).

Johnstone, Di Francesco & Kirk (2004) showed that the majority of cores in L1688 are found in the central region, and are covered in this study.

The completeness limit of our data can be estimated using the measured sensitivity of the map, together with the average size of the detected cores. The latter because more mass can be hidden in the noise if the source is larger. In practice this can be done by scaling the integrated flux density from a number of well detected objects, down to the level where the sources would be just undetected, taking into account the selection criteria. For more details of this technique, see Nutter & Ward-Thompson (2007). The completeness limit of our map was found to be $0.1 M_{\odot}$. As an additional check on this limit, we added synthetic sources to the map in a Monte Carlo fashion and attempted to recover them using the method described above. We found that for source sizes up to $20''$ we recovered all of the sources and for sources up to $30''$ we recovered 90%.

4 CORE MASSES

We assume the 850μm integrated flux density is optically thin and so the masses of the cores are calculated using the following equation:

$$M = \frac{S_{850} D^2}{\kappa_{850} B_{850,T}}, \quad (1)$$

where S_{850} is the 850 μm flux density, D is the distance to the source, κ_{850} is the mass opacity of the gas and dust, and $B_{850,T}$ is the Planck function at temperature T (Kirk, Ward-Thompson, & André 2005). Temperatures for each of the regions in the cloud are given in Table 3. We calculate the masses using the revised temperatures given by Stamatellos, Whitworth, & Ward-Thompson (2007), hereafter SWW07.

MAN98 assumed a value for dust mass opacity of $\kappa_{1.3mm} = 0.005 \text{ cm}^2 \text{g}^{-1}$ for prestellar cores (Preibisch et al.

Table 3. Assumed dust temperatures (T_{dust}) in K of the regions in the Ophiuchus cloud from MAN98 and SWW07.

Region	MAN98	SWW07
Oph-A	20	11
Oph-B	12	10
Oph-C	12	10
Oph-E	15	10
Oph-F	15	10
Oph-J	—	10

1993; Andre, Ward-Thompson, & Motte 1996). This is extrapolated to 850μm using the wavelength dependence factor, β , which is assumed have a value of 2 in the submillimetre (Hildebrand 1983). We thus obtain a dust opacity value of $\kappa_{850} = 0.01 \text{ cm}^2 \text{g}^{-1}$.

SWW07 estimated the dust temperatures of clumps in Ophiuchus. They found that in regions where prestellar cores are observed, temperatures of 10-11K are to be expected. Specifically they suggest a dust temperature of 10K for all the main regions identified by this study. The exception to this value is Oph-A, containing SM1 (see Table 3).

For this study we shall assume a distance of 139 ± 6 pc to the Ophiuchus cloud (Mamajek 2008). This value was determined using Hipparcos data and reddening studies (Chini 1981; de Geus, de Zeeuw, & Lub 1989; Knude & Hog 1998). Using these new parameters for distance and temperature a new CMF for the region was created.

5 CORE MASS FUNCTION

In this section we describe CMFs constructed from the above data. We first compare these with previous work, and then see what can be learnt from our new analysis.

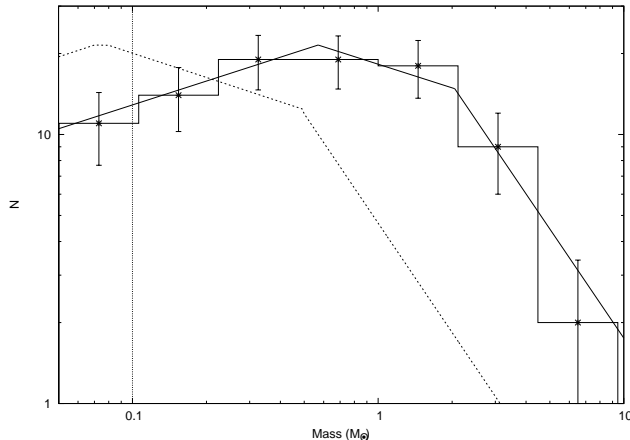


Figure 6. CMF for the Ophiuchus dark cloud. The completeness limit is shown at a dashed vertical line at $0.1M_{\odot}$. A three part stellar IMF (see text), normalised to the peak in N of the CMF, is overlaid as a dotted line. The three power-law slopes of the IMF are also shown fitted to the data as solid black lines, now normalised in M .

5.1 Comparison with Previous Work

5.1.1 MAN98

Figure 5 shows the data from this study plotted in the same way as the mass spectrum from MAN98, which has been recreated for comparison. Good agreement is seen. Both datasets show the same power law slopes. Below about $2M_{\odot}$ in our data, the slope in the power law decreases from -1.35 to -0.3 (see section 5.2). This is in approximate agreement with the MAN98 results which place this ‘knee’ in the high-mass end of the spectrum at approximately $0.5M_{\odot}$. The difference in the location of the ‘knee’ is explained by the difference in the temperatures and distances assumed by the two studies (see Table 3).

Our mass spectrum also shows another decline in the slope at lower masses in the mass range up to $0.7M_{\odot}$ (Figure 5). This effect is seen here, 7 times above our completeness limit, and represents a power law equivalent to the low-mass slope of the stellar IMF.

5.1.2 Johnstone et al. 2000

Johnstone et al. (2000) produced a cumulative CMF for L1688 using some of the same scan-map data (see their Figure 7). Once again, good agreement is seen. Their CMF shows similarities with the two higher-mass slopes of the stellar IMF, in agreement with this study. This earlier study’s completeness limit of approximately $0.4M_{\odot}$ prevents comparison at lower masses.

The CMF produced by Johnstone et al. (2000) shows a ‘knee’ at around $0.8M_{\odot}$. As with the MAN98 study, this feature is also seen in our data when an adjustment is made for the different temperature assumptions of the two studies.

5.1.3 Stanke et al. 2006

Stanke et al. (2006) mapped the L1688 region at 1.2mm using IRAM. They produced a mass spectrum with a similar form to that produced in Figure 5b above. Stanke et al.

(2006) surveyed 111 starless cores. Although this outnumbers the cores identified in this study, many of these are extended, low surface brightness objects that may not be gravitationally bound. They concluded that regardless of the details, the CMF resembles the shape of the IMF with three power-law slopes presented in their CMF plot.

Stanke et al. (2006) also show the ‘knee’ and a tentative turnover in their CMF. The positions of these feature are not well constrained but their locations at $0.5-1.0M_{\odot}$ and $0.1-0.3M_{\odot}$, respectively, are approximately consistent with our data.

5.1.4 Enoch et al. 2008

Enoch et al. (2008) surveyed Perseus, Serpens, and Ophiuchus by comparing Bolocam 1.1mm continuum emission maps with Spitzer c2d surveys. Our CMF is consistent with theirs (see their Figure 13).

5.2 Our Data

The 72 cores in our data with no infrared association are used to plot the CMF in Figure 6. The dashed vertical line is the 5σ completeness limit of $0.1M_{\odot}$ in our map. This is an improvement over the MAN98 completeness limit, which is due mainly to the better resolution and sensitivity at $850\mu\text{m}$ provided by the complete SCUBA data.

Figure 6 shows our CMF. The dotted line shows the stellar IMF, normalised, in N , to the peak of the CMF. The dotted line is a fit to the power laws of the CMF as outlined below. Cores noted to have an infrared source associated with their position in Table 2 are not included. Compared with Figure 5, this representation of the data uses a simple number count of cores as opposed to a count divided by the bin size. Figure 6 demonstrates that the data are consistent with the three power-laws in the stellar IMF.

This is the first time that the full turnover in the CMF has been seen in Ophiuchus. Here it is seen at $0.7M_{\odot}$. The only other cloud for which this turnover has been detected is Orion (Nutter & Ward-Thompson 2007). To compare the CMF to the stellar IMF we use a stellar IMF with a power law of the following form:

$$M \frac{dN}{dM} \propto M^{-x}, \quad (2)$$

where x takes on different values in different mass regimes. For the stellar IMF we assume the following exponents:

$$\begin{aligned} x &= 1.35, & 0.5M_{\odot} &< M, \\ x &= 0.3, & 0.08M_{\odot} &< M < 0.5M_{\odot}, \\ x &= -0.3, & 0.01M_{\odot} &< M < 0.08M_{\odot}. \end{aligned} \quad (3)$$

The higher mass end values for x are taken from Kroupa (2002). Below $0.08M_{\odot}$ the IMF is based on fits to young cluster populations used in (Chabrier 2003). In this study values between 0.2 and 0.4 are found, so an average of 0.3 is used here.

5.3 Star Formation Efficiency

The striking similarity between the CMF and the stellar IMF that is seen in the Ophiuchus L1688 cloud, once again

Table 4. Masses and sizes for cores in the Oph-A and Oph-B regions of the L1688 core. Given the assumption outlined in the text, the error in the masses is $\pm 10\%$ (see Section 2).

Core Name	Mass (M_{\odot})	Size (AU x AU)
A-MM1	0.09	Unresolved
A-MM2/3	0.16	2800 x 1900
A-MM4	0.48	2100 x 2100
A-MM5	0.82	2800 x 2500
A-MM6	2.10	3600 x 2500
A-MM7	0.92	3300 x 2200
A-MM8	3.18	2200 x 1900
A-MM11	0.64	5600 x 1900
A-MM12	0.45	Unresolved
A-MM16	0.03	Unresolved
A-MM17	0.03	1900 x 1900
A-MM18	0.87	4200 x 2800
A-MM20	0.12	Unresolved
A-MM21	0.21	Unresolved
A-MM22	0.11	2800 x 2200
A-MM23	1.50	4900 x 2100
A-MM26	0.43	3100 x 1900
A-MM27	0.34	4200 x 1900
A-MM28	0.18	2500 x 1900
A-MM29	0.16	Unresolved
A-MM30	1.28	4400 x 1900
A2-MM1	0.33	3300 x 1900
A3-MM1	0.33	2500 x 2200
A-N	0.21	Unresolved
A-S	0.01	2100 x 1900
SM1	7.35	6100 x 1900
SM1N	2.91	2500 x 1900
SM2	5.97	5100 x 3600
VLA1623	2.93	4200 x 2500
B1-MM1	0.02	Unresolved
B1-MM2	0.63	3100 x 1900
B1-MM3	2.61	2800 x 2500
B1-MM4	2.10	5000 x 3200
B1-MM6	0.22	2500 x 1900
B1-MM7	0.11	1900 x 1900
B1B2-MM1	0.22	5600 x 2200
B2-MM2	0.88	3300 x 2200
B2-MM4	0.96	Unresolved
B2-MM5	1.14	3600 x 2500
B2-MM6	1.62	5000 x 4200
B2-MM7	0.62	4200 x 2800
B2-MM8	1.63	2800 x 2500
B2-MM9	1.37	3900 x 1900
B2-MM13	0.49	3100 x 2800
B2-MM14	1.26	4400 x 2100
B2-MM15	0.62	Unresolved
B2-MM16	1.31	2500 x 2200

gives a strong indication that the form of the IMF is determined at the prestellar core stage. Furthermore, we have traced this similarity to lower masses than was previously possible. This has allowed us to determine the turnover mass in the core mass function.

If it is assumed that each core will form a single star with a fixed star formation efficiency (ϵ) for all cores, then the CMF can be used to predict an output IMF. In this case the best fit is obtained with $\epsilon = 0.2$ (see Figure 7). This is a

Table 5. Masses and sizes for cores in the Oph-C, Oph-E, Oph-F and Oph-J regions of the L1688 core. Given the assumption outlined in the text, the error in the masses is $\pm 10\%$ (see Section 2).

Core Name	Mass (M_{\odot})	Size (AU x AU)
C-MM2	1.11	Unresolved
C-MM3	1.42	4200 x 3300
C-MM5	1.24	Unresolved
C-MM6	1.05	6700 x 3300
C-MM8	0.15	Unresolved
C-MM9	0.06	2200 x 2100
C-MM10	0.37	2400 x 1900
C-MM12	0.09	4400 x 2400
C-N	1.60	4700 x 3800
E-MM2a	0.12	1900 x 1900
E-MM2b	0.16	3100 x 2500
E-MM2d	0.41	Unresolved
E-MM4	0.31	3600 x 3100
E-MM5	0.28	2800 x 2100
E-MM8	0.19	3100 x 1900
F-MM1	1.05	4200 x 2400
F-MM2a	1.11	4400 x 3800
F-MM6	0.10	Unresolved
F-MM8	0.21	Unresolved
F-MM9	0.10	Unresolved
J-MM2	0.42	4700 x 3200
J-MM3	0.34	3900 x 2500
J-MM4	0.17	Unresolved
J-MM5	0.16	Unresolved
J-MM6	0.07	Unresolved

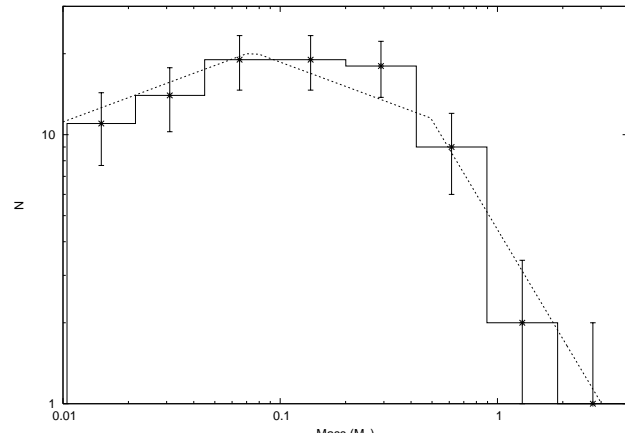


Figure 7. CMF for the L1688 core multiplied by a star formation efficiency factor of 0.2, assuming each core forms a single star. A three part stellar IMF, normalised to the peak in N of the CMF, is overlaid as a dotted line (see text for details).

simplistic model, and the shape of the CMF does not change as a function of ϵ .

A more sophisticated approach than ‘one core, one star’ would be to model the transformation between core masses and stellar masses in a way that produces multiple stars from each core (Hatchell & Fuller 2008; Swift & Williams 2008). Goodwin et al. (2008) discuss what they call the ‘fully multiple star model’. This model assumes that

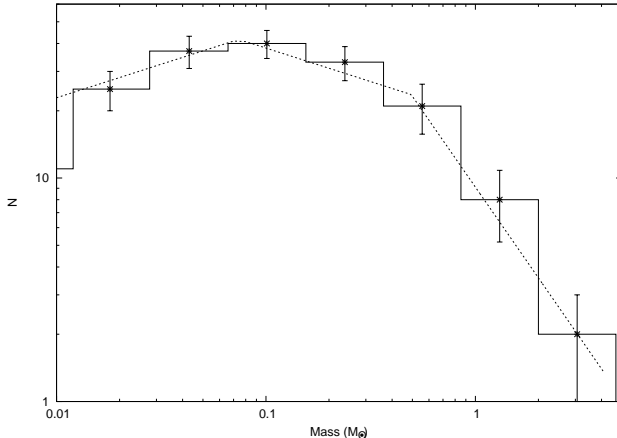


Figure 8. Potential stellar IMF for the L1688 core, modelled using the ‘fully multiple star model’ from Goodwin et al. (2008) shown as a histogram. The real stellar IMF is shown as a dotted line. See text for details.

cores with masses lower than a certain mass, M_{CRIT} , will form binary systems and larger cores will form binary or multiple systems. $M_{CRIT} = \epsilon M_{KNEE}$, where M_{KNEE} is the location of the ‘knee’ in Figure 6 (see also Goodwin, Whitworth, & Ward-Thompson 2004). Thus for this study we use $M_{CRIT} = 2\epsilon M_{\odot}$.

Using the ‘fully multiple star model’ it is possible to transform the CMF in Figure 6 to produce a potential, future stellar IMF for L1688 – see Figure 8. This plot shows very good agreement with the real stellar IMF. The best fit model here requires $\epsilon = 0.4$.

It is important to remember that this is the star formation efficiency within gravitationally bound cores, and so a high value is to be expected. The total mass of prestellar cores in L1688 is $29.3 M_{\odot}$. The total mass of the L1688 cloud complex is $1447 M_{\odot}$ (Loren 1989). Coupling this to our value of $\epsilon = 0.4$ for the prestellar cores gives a value for the absolute star formation efficiency of the central portion of the L1688 cloud of about 1-2%.

5.4 Comparison with Orion

Nutter & Ward-Thompson (2007) used the SCUBA data archive to produce a CMF for the Orion molecular cloud and found a turnover in the CMF at $1.3 M_{\odot}$. This is a factor of two higher than the CMF turnover seen here at $0.7 M_{\odot}$ in the L1688 cloud. However we note that the difference is not significantly greater than one bin-width. Hence, studies with larger number statistics will be needed to verify this hypothesis (Ward-Thompson et al. 2007b).

The instrumentation and methodology for deriving the properties of cores is the same in both studies. Both regions can be modelled using the method described in the previous section (Goodwin et al. 2008), but only by using different values for the SFE. These results suggest that the position of the turnover in the CMF may vary with the environment in which the cores reside.

6 CONCLUSIONS

In this paper we have re-analysed the SCUBA archive data for L1688, incorporating all available high signal-to-noise scan-map and jiggle-map data. An updated form of the CMF in the L1688 cloud complex has been presented using updated values for the distance to this region as well as new estimates for the temperatures of the cores.

We have shown that the CMF for L1688 is consistent with a three part power-law with slopes the same as seen in the stellar IMF. The higher-mass end of the CMF declines as a power law which is consistent with other studies of L1688 (MAN98; Johnstone et al. 2000; Stanke et al. 2006) as well as studies of Orion (Nutter & Ward-Thompson 2007; Motte et al. 2001; Johnstone et al. 2001; Johnstone, Matthews, & Mitchell 2006).

Hence, the results are mostly in agreement with those found in earlier studies. However, our deeper maps have allowed the discovery of a turnover in the CMF at $0.7 M_{\odot}$ which shows that the core mass function continues to mimic the stellar initial mass function to low masses. This agreement is indicative that the stellar IMF is determined at the prestellar core stage.

It has been shown that the relationship between the CMF and IMF is not necessarily a simple 1:1 translation in the mass axis. Consistency can also be achieved using a fully multiple star model.

ACKNOWLEDGMENTS

The James Clerk Maxwell Telescope is operated by the Joint Astronomy Centre, Hawaii, on behalf of the UK STFC, the Netherlands NWO, and the Canadian NRC. SCUBA was built at the Royal Observatory, Edinburgh. RJS acknowledges STFC studentship support whilst carrying out this work.

REFERENCES

- Archibald E. N., et al., 2002, MNRAS, 336, 1
- Andre P., Deeney B. D., Phillips R. B., Lestrade J.-F., 1992, ApJ, 401, 667
- Andre P., Ward-Thompson D., Motte F., 1996, A&A, 314, 625
- Barsony M., Kenyon S. J., Lada E. A., Teuben P. J., 1997, ApJS, 112, 109
- Bertiau F. C., 1958, ApJ, 128, 533
- Bertout C., Robichon N., Arenou F., 1999, A&A, 352, 574
- Casanova S., Montmerle T., Feigelson E. D., Andre P., 1995, ApJ, 439, 752
- Chabrier G., 2003, PASP, 115, 763
- Chini R., 1981, A&A, 99, 346
- Di Francesco J., Evans N. J. II, Caselli P., Myers P. C., Shirley Y., Aikawa Y., Tafalla M., 2007, prpl.conf, 17
- Di Francesco J., Johnstone D., Kirk H., MacKenzie T., Ledwosinska E., 2008, ApJS, 175, 277
- Emerson D. T., Payne J. M., 1995, ASPC, 75
- Enoch M. L., Evans N. J. II, Sargent A. I., Glenn J., Rosolowsky E., Myers P., 2008, arXiv, 805, arXiv:0805.1075

Goodwin S. P., Whitworth A. P., Ward-Thompson D., 2004, A&A, 419, 543

Goodwin S. P., Nutter D., Kroupa P., Ward-Thompson D., Whitworth A. P., 2008, A&A, 477, 823

Greene T. P., Young E. T., 1992, ApJ, 395, 516

de Geus E. J., de Zeeuw P. T., Lub J., 1989, A&A, 216, 44

Hatchell J., Fuller G. A., 2008, A&A, 482, 855

Hildebrand R. H., 1983, QJRAS, 24, 267

Jenness T., Holland W. S., Chapin E., Lightfoot J. F., Duncan W. D., 2000, ASPC, 216, 559

Jenness T., Lightfoot J. F., Holland W. S., Greaves J. S., Economou F., 2000, ASPC, 217, 205

Jessop N. E., Ward-Thompson D., 2001, MNRAS, 323, 1025

Johnstone D., Wilson C. D., Moriarty-Schieven G., Joncas G., Smith G., Gregersen E., Fich M., 2000, ApJ, 545, 327

Johnstone D., Fich M., Mitchell G. F., Moriarty-Schieven G., 2001, ApJ, 559, 307

Johnstone D., Di Francesco J., Kirk H., 2004, ApJ, 611, L45

Johnstone D., Matthews H., Mitchell G. F., 2006, ApJ, 639, 259

Jorgensen J., Johnstone D., Kirk H., Myers P., Allen L., Shirley Y., 2008, arXiv, 805, arXiv:0805.0599

Kirk J. M., Ward-Thompson D., André P., 2005, MNRAS, 360, 1506

Knude J., Hog E., 1998, A&A, 338, 897

Kroupa P., 2002, Sci, 295, 82

Leous J. A., Feigelson E. D., André P., Montmerle T., 1991, ApJ, 379, 683

Loren R. B., 1989, ApJ, 338, 902

Mamajek E. E., 2008, AN, 329, 10

Montmerle T., Koch-Miramond L., Falgarone E., Grindlay J. E., 1983, ApJ, 269, 182

Motte F., André P., Neri R., 1998, A&A, 336, 150

Motte F., André P., Ward-Thompson D., Bontemps S., 2001, A&A, 372, L41

Nutter D., Ward-Thompson D., 2007, MNRAS, 374, 1413

Nutter D., Ward-Thompson D., André P., 2006, MNRAS, 368, 1833

Onishi T., Mizuno A., Kawamura A., Tachihara K., Fukui Y., 2002, ApJ, 575, 950

Preibisch T., Ossenkopf V., Yorke H. W., Henning T., 1993, A&A, 279, 577

Salpeter E. E., 1955, ApJ, 121, 161

Sandell G., 1994, MNRAS, 271, 75

Sandell G., Jessop N., Jenness T., 2001, Starlink Cookbook, 11.2

Stamatellos D., Whitworth A. P., Ward-Thompson D., 2007, MNRAS, 379, 1390

Stanke T., Smith M. D., Gredel R., Khanzadyan T., 2006, A&A, 447, 609

Swift J. J., Williams J. P., 2008, ApJ, 679, 552

Tachihara K., Onishi T., Mizuno A., Fukui Y., 2002, A&A, 385, 909

Testi L., Sargent A. I., 1998, ApJ, 508, L91

Tilanus R. P. J., Jenness T., Economou F., Cockayne S., 1997, ASPC, 125, 397

Vrba F. J., 1977, AJ, 82, 198

Ward-Thompson D., Robson E. I., Whittet D. C. B., Gordon M. A., Walther D. M., Duncan W. D., 1989, MNRAS, 241, 119

Ward-Thompson D., Scott P. F., Hills R. E., André P., 1994, MNRAS, 268, 276

Ward-Thompson D., Motte F., André P., 1999, MNRAS, 305, 143

Ward-Thompson D., 2002, Sci, 295, 76

Ward-Thompson D., André P., Crutcher R., Johnstone D., Onishi T., Wilson C., 2007a, Protostars and Planets V

Ward-Thompson D., et al., 2007b, PASP, 119, 855

Wilking B. A., 1992, lmsf.book, 159

Wilking B. A., Lada C. J., 1983, ApJ, 274, 698

Wilking B. A., Lada C. J., Young E. T., 1989, ApJ, 340, 823

Zinnecker H., McCaughrean M. J., Wilking B. A., 1993, prpl.conf, 429